Spectroscopy and dynamics of isolated anions: Versatile instrumentation for photodetachment and photoelectron spectroscopy

Eleanor K. Ashworth, Stephen H. Ashworth, and James N. Bull[a)]
School of Chemistry, University of East Anglia, Norwich, NR4 7TJ, United Kingdom

Molecular anions are appealing targets for study because, compared with their neutral and cationic counterparts, they can be probed with conventional laboratory lasers without the need for multiphoton ionization schemes and they provide spectroscopic details on the corresponding neutral molecules. Here, we describe a section of a modular instrument designed to perform high-throughput photoelectron and photodetachment spectroscopy of gas-phase anions, with future provision for time-resolved and isomer-selective spectroscopy. The instrument framework allows for the incorporation and adaptation of several ion sources, here demonstrated with plasma (electric) discharge sources providing variable hard to soft ion generation conditions. The generated anions are separated according to their mass-to-charge ratio through time-of-flight (ToF) mass spectrometry ($\frac{m/z}{\Delta m/z} = 500\text{--}600$) and are focussed into a set of perpendicular velocity-map imaging (VMI) electrodes ($\frac{\Delta E}{E} \approx 4\%$), where mass-selected anions are probed using laser light and the ejected electrons are velocity-map imaged. Instrument performance is demonstrated through acquisition of photodetachment and photoelectron spectra for CH_2CN^-, showing sharp resonances in the vicinity of the detachment threshold assigned to rovibrational states of a dipole-bound anion, and broader lifetime-limited spectral features at photon energies well above threshold assigned to prompt autodetachment from a temporary anion resonance. Similar measurements could be performed on any molecular anions generated in the sources.

I. INTRODUCTION

Scientific instruments designed to investigate the spectroscopy and dynamics of gas-phase molecular anions are predominantly based on photodetachment and/or photoelectron spectroscopies,[1–5] where photodetachment spectroscopy records total electron yield as a function of wavelength (or photon energy), and photoelectron spectroscopy involves measuring the kinetic energy of ejected electrons. Combined, these two spectroscopic strategies can provide unparalleled insight into the electronic structure of a target anion and corresponding neutral molecule. Furthermore, through analyzing trends in photoelectron spectra and associated angular distributions as a function of wavelength, for example as a 2D map, indirect fingerprints of autodetachment and internal conversion dynamics can be obtained to infer (above threshold) excited-state dynamics of the selected anion.[1,6]

Our understanding of the spectroscopy and dynamics of isolated anions has significantly evolved over the last two or so decades,[4,7] assisted by developments in instrumental techniques, including velocity-map imaging,[8] electrospray ionization,[3] and cryogenic ion trapping,[9,10] the availability of broad tunability lasers (optical parametric oscillators, OPOs), and femtosecond/picosecond lasers offering time-resolved spectroscopy.[11] These developments have facilitated the study of small (a few atom) anions to multiply-charged anions[12] and large biologically-relevant and cluster anions generated through electrospray ionization,[13–15] allowing detailed characterisation of excited-state reaction dynamics,[16,17] internal conversion and properties of

non-valence states,[18,19] and high-resolution spectroscopic properties and characterization of molecular orbitals and photoelectron angular distributions.[20,21] There is a need for new instrumental platforms with scope for development through the incorporation of new anion preparation and selection strategies.

A cornerstone in the development of modern anion photoelectron spectroscopy was the emergence of velocity-map imaging (VMI) in 1997.[22] Prior to VMI, electron kinetic energy (eKE) distributions in photoelectron spectroscopy were recorded using electrostatic energy analyzers or a magnetic bottle assembly, which, while potentially offering good spectral resolution and limited (manual) angular information,[23] suffer from discrimination effects towards certain eKE ranges (notably near-zero eKE). On the other hand, VMI offers an instrumentally simpler detection strategy able to record all eKEs[24,25] and acquires all angular information simultaneously, making it the obvious choice for new instruments. More sophisticated VMI assemblies, such as SEVI (slow photoelectron velocity-map imaging),[26] provide spectral resolution comparable with, or better than, magnetic bottle spectrometers.

This paper reports the photodetachemnt and photoelectron section of an action spectroscopy instrument: PASTA (Photoinduced Action Spectroscopy Targeting Anions). The instrument is shown in FIG. 1, and was developed with the following remit:

- Capabilities to perform both photodetachment (resolution limited by laser bandwidth) and photoelectron spectroscopies on anions, and to record photoelectron spectra simultaneously when acquiring a photodetachment spectrum (i.e. frequency-resolved photoelectron spectroscopy);

- The versatility to generate ions from easily-
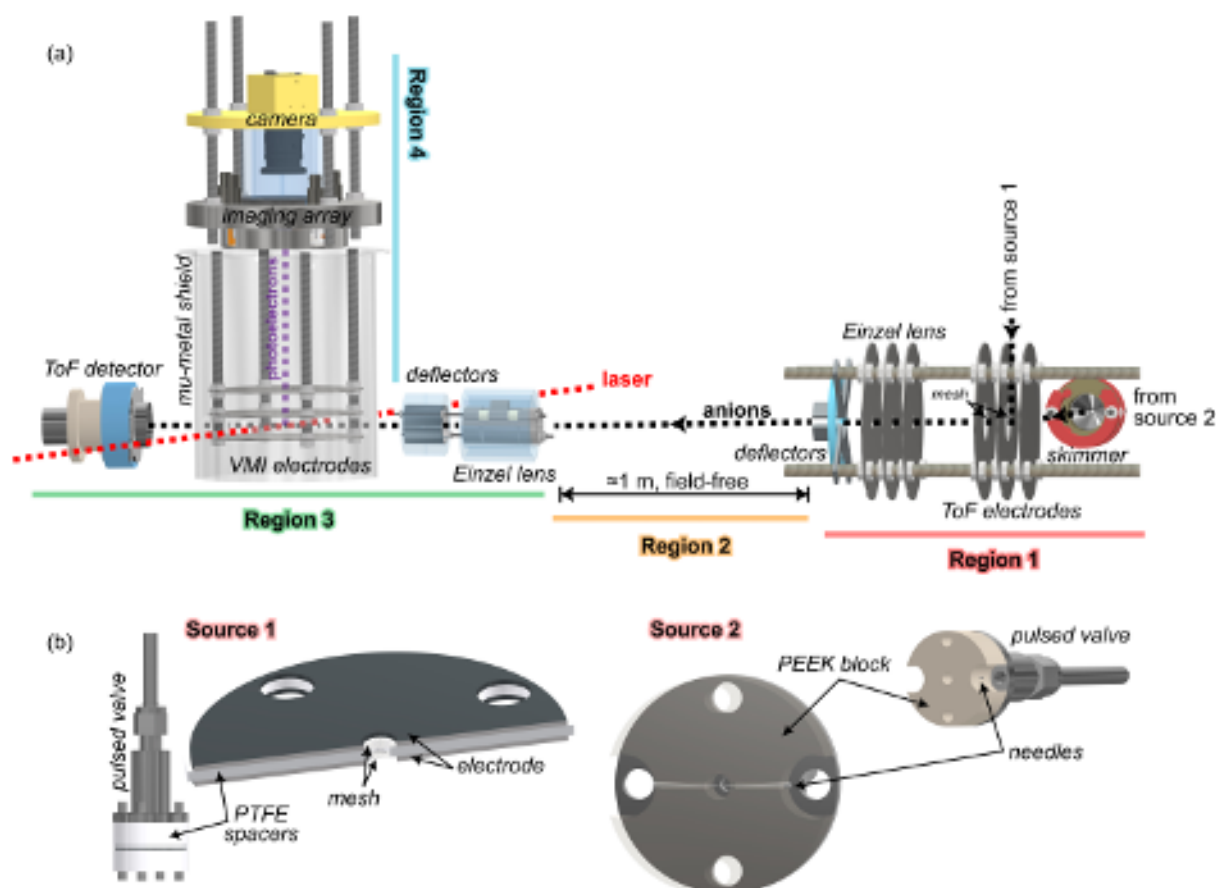
a)Electronic mail: james.bull@uea.ac.uk

FIG. 1. Illustrations of (a) the photoelectron/detachment section of the PASTA instrument, and (b) illustrations of the two pulsed valve sources. (a) The four instrument regions are: (**1**) ion source and time-of-flight (ToF) extraction region, (**2**) field-free ToF drift region (length ≈ 1 m), (**3**) ion–laser interaction and ion detection region, and (**4**) the velocity-map imaging assembly (chevron dual-MCP $\rightarrow$ P43 phosphor $\rightarrow$ CMOS camera). A ToF detector is positioned after the VMI assembly. Source 1 is positioned perpendicular to the ToF electrodes above the plane of the instrument, while source 2 is positioned perpendicular to the ToF electrodes in the plane of the instrument. (b) In pulsed valve source 1, the sample gas is passed through the central hole in two electrodes (each of which are covered by nickel meshes – the first at >-0.2 kV and second at 0 V), producing a hard plasma during the gas pulse. In pulsed valve source 2, a softer plasma is produced by pulsing the precursor gas over two needles (>-0.5 and 0 kV), with an optional skimmer placed a few centimetres after the plasma source to collimate the beam. Illustrations are not to scale (see text for dimensions).

interchangeable hard- and soft-plasma pulsed valve sources. Using these pulsed valve sources, the instrument should be capable of studying small anions (a few atoms) to moderately-sized anions (≈ 60 atoms) through time-of-flight mass spectrometry;

- Velocity-map imaging detection to acquire electron kinetic energies without discrimination effects, and to record angular information of photoelectrons;

- The capacity to disentangle prompt and delayed (e.g. thermionic emission) signals in both photoelectron and photodetachment spectra by time-gating the photoelectron detector (≈ 5 ns time resolution) relative to the laser;

- Future provision for coupling with electrospray ionization, tandem ion mobility spectrometry and ion trapping, allowing for photoisomerization action spectroscopy, isomer-specific photodetachment and photoelectron spectroscopies (in both frequency and femto- to picosecond time domains), and photogeneration, separation, and study of transient intermediates that survive for a few milliseconds or longer.

We demonstrate photodetachment and photoelectron spectroscopy capabilities through studying jet-cooled CH_2CN^- over the $11,500$–$24,000$ cm^{-1} range (a range spanning almost 425 nm), which involved accumulating velocity-map images at more than 5000 wavelengths using an optical parametric oscillator (OPO) laser.

II.   INSTRUMENT DESIGN

A cut-away diagram of the instrument is shown in FIG. 1. The instrument is divided into four regions (**1**–**4**), which are described in the following subsections, and is predominately based on 6" and $2^3/4$" ConFlat flanges. The vacuum pumping framework combines five turbo-molecular pumps (4× Leybold Turbovac 350 i(X) and a Varian Turbo-V 250) and four oil-free backing pumps (Leybold Scrollvac 7 plus and 15 plus). This configuration achieves baseline pressures of 10^8–10^{-9} mbar in the detector regions. The entire instrument is mounted on a frame constructed from RS Components 40×40 mm and 20×20 mm aluminium extrusion, which provided a simple railway assembly for each chamber.

Our design makes use of 3D-printed components, which lowered production costs significantly and allowed complexly-shaped holders to be fabricated in a matter of hours. These 3D-printed components are mainly supports or enclosures, such as for mounting electrodes. Most of the 3D-printed components were made from polylactic acid (PLA), with any components situated inside chambers (i.e. under vacuum) printed with 100% infill to minimise out-gassing. During the build, we found that the incremental addition of PLA components into the vacuum chambers did not substantially increase the evacuation time to reach operating conditions, indicating that PLA out-gassing was not a significant/limiting factor. We note that the surface of any PLA element can be made conductive by coating with Aquadag or Graphit 33 spray graphite, minimising any electrostatic charging issues. We also note that PEEK is available to be 3D printed and, generally, is a more desirable vacuum material.

The synchronization and event timing of the instrument is controlled with a Quantum Composers model 9528 TTL pulse generator (and also secondary BNC 575 pulse generator), providing 250 ps timing resolution and <50 ps channel-to-channel jitter. A typical pulsing sequence for a single-colour experiment using a flash-lamp based laser (nanosecond duration light pulses) is outlined in FIG. 2. The instrument is designed to operate at either 10, 20, or 40 Hz, as defined by the operating frequency of Nd:YAG and OPO lasers, and by the repetition rate of a future ion mobility sector. The velocity-map imaging acquisition, laser wavelength and measured fluence, and ToF spectrum recording is controlled by a LabVIEW 2019 interface.

A.   Pulsed valve plasma sources

There are a wide range of ion sources available to generate molecular anions; the target molecules accessible in an experiment are ultimately defined by the compatible ion sources. Broadly speaking, suitable sources for ion spectroscopy experiments can be divided into hard and soft ionization sources,[29] where the former generates
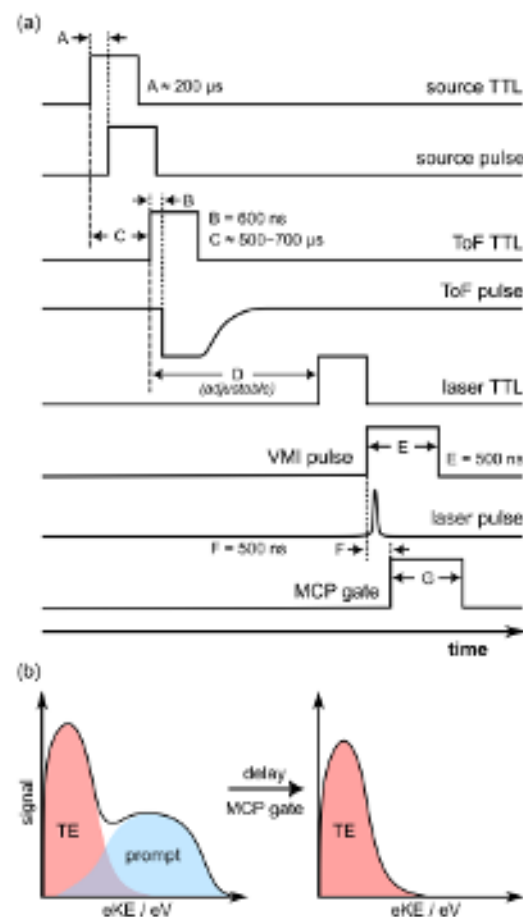

FIG. 2.   Timing sequence for anion formation, extraction, and laser interaction. (a) The source TTL triggers the pulsed valve. **A** is the delay between the trigger and plasma ignition due to opening of the valve. The ToF TTL triggers the Behlke switches driving the ToF electrodes and sets $t = 0$ in the ToF spectrum. **B** is the turn-on time delay of the switches and **C** is an adjustable delay to allow the ions to reach the center of the ToF electrodes. **D** is an adjustable delay between the laser TTL trigger and the ToF TTL, allowing the laser pulse to interact with the m/z of interest. The VMI TTL (pulse width = **E**) triggers the VMI electrodes, which energise a few nanoseconds before the laser intersects the anions. The second MCP of the VMI detector is connected to a gating unit (described in the text), which can be delayed (**F**) relative to the VMI. (b) Schematic diagram illustrating the presence of prompt and delayed [thermionic emission (TE)] detachment signal in a photoelectron spectrum. By delaying the MCP gate (width **G**, tens of ns) pulse by some tens of nanoseconds, prompt and delayed detachment signals can be disentangled. As detailed in Refs 27 & 28, TE occurs when an excited electronic state of the anion internally converts back to the ground electronic state and, eventually, ejects an electron in a statistical manner (hundreds of nanoseconds to milliseconds) after intramolecular internal energy redistribution. By measuring TE signal as a function of wavelength, internal conversion dynamics can be fingerprinted.

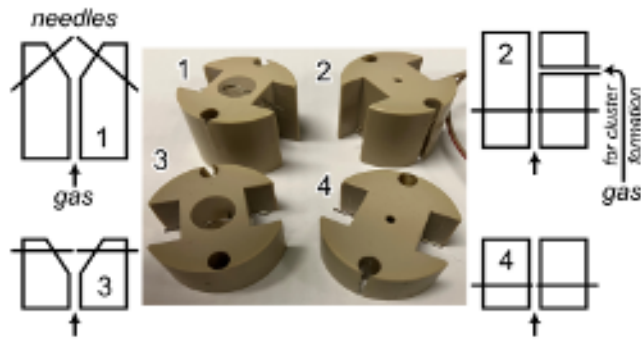extensive fragmentation (and often molecular rearrange-

FIG. 3. Photograph of several manufactured PEEK blocks designed for the needle-based plasma sources,[30,31] with corresponding profiles. PEEK is easily machined, allowing swappable blocks with modified recombination and jet-cooling properties (e.g. bore diameter and conical cross section), needle position, or to include a capillary inlet (before or after the plasma needles) to introduce other gases (e.g. water vapour) to form anion-neutral clusters. The PEEK blocks are attached to the pulsed valve with threaded rod.

ments and ion-molecule reactions), while the latter (e.g. electrospray ionization) is suited for introducing larger or more fragile ions, such as bio- or macromolecules, into the gas phase where the focus of study is the parent anion. In the current deployment, anions are produced using one of two pulsed-valve based plasma sources (FIG. 1b). Both sources combine a Parker-Hannifin series 9 pulse valve with custom plasma and recombination regions in a polyether ether ketone (PEEK) block, with the blocks easily swapped to vary the hardness of the plasma. For both plasma sources, the molecule of interest is introduced from the gas inlet system (FIG. S2) using a mixture of $\approx$1% molecule of interest and $\approx$99% Ar or N_2. While pulsed-type sources are most desirable because of supersonic expansion and jet cooling, the instrument is equally suited for continuous (effusive) sources; although, in such a case, the system would benefit from an increase in the pumping provision.

In our hard plasma source (FIG. 1b, source 1), which is positioned perpendicular to (and above) the ToF electrodes, the plasma volume is defined by two fine nickel meshes (88% transmission, TWP Inc.) in a 3 mm bore separated by PTFE spacers ($\approx$1 mm thickness) and a PEEK recombination region ($\approx$10 mm length). The design is loosely based on that reported in Ref. 32. The plasma is generated when gas pulses through the meshes because the first is held at a high negative voltage relative to the first (grounded). The most stable plasmas are generated when the voltage is only slightly above the discharge threshold, and when the power supply is buffered with a RC circuit (e.g. 4.7–30 kΩ, 20 nF). Ions generated in the plasma (estimated at $\approx$10^7–10^9 anions across all m/z per pulse) then pass through the recombination zone and undergo supersonic expansion and jet cooling into the vacuum chamber. The source is useful

for generating atomic species such as C^-, O^-, and N^-, or halogen anions for calibrating the VMI assembly and, with higher backing pressures or sample concentrations, readily produces polyatomic species. The harsher conditions created in this plasma mean that this source requires more regular maintenance, compared with source 2. In the future, the plasma region of this source could easily be interchanged with an electron impact ionization source, if desired.

The softer plasma source (FIG. 1b, source 2), positioned perpendicular to the ToF electrodes, has a pair of needles ($<$1 mm diameter, $<$1 mm separation) directed towards each other in a PEEK block. The simplicity of this source and the ease with which different geometries can be fabricated (FIG. 3) allows the properties of the plasma generation, ion-molecule recombination, or seeding of other neutral molecules to be easily adapted, thus facilitating the generation of a wide range of molecular and cluster anions. The plasma generated by the source is mostly stable (maintenance/cleaning requirements depend on the initial sample), and we are able to acquire a full week or two of experimental data without needing to clean the source. A full summary of these capabilities will be the subject of a forthcoming publication. An optional skimmer situated $\approx$20 mm after the PEEK block is available to select the coolest part of the supersonic expansion. We note that similar pulsed valve sources combined with needle electrodes[30,31] have been used for the generation of both large neutral molecules[33,34] and complexes.[35] Our design offers the advantage of straightforward adaptation to different samples and plasma conditions.

B. Time-of-flight mass spectrometry

Anions are separated based on their mass-to-charge ratio (m/z) through time-of-flight (ToF) mass spectrometry utilizing a Wiley-McLaren configuration.[36] The ToF electrodes consist of a repeller ($V_{rep} > 2$ kV), an extractor ($V_{ext} \approx 0.75V_{rep}$), and the ground, each separated by 10 mm. Electrodes were laser cut to have a 80 mm diameter from 1.2 mm thickness low-magnetic stainless steel. The extractor and ground electrodes have 20 mm apertures covered with a fine nickel mesh (88% transmission, TWP Inc.), affixed with a vacuum-compatible conductive epoxy. Target anions are injected between the repeller and extractor electrodes (20 Hz in this work), which are initially grounded, and are then pulsed to high voltage using a pair of Behlke HTS-60-02 high voltage transistor switches (see FIG. S3). The switch drive circuits were tuned to provide a rise time of $\approx$8 ns. After ions are accelerated by the ToF electrodes, they pass through a three-electrode Einzel lens (≈ -300 V on the central electrode) to collimate the beam, followed by sets of deflectors (X_1/X_2 and Y_1/Y_2) controlled by $\pm$120 V power supplies to provide ion beam steering. The anions then separate according to their m/z in a field-free flight

region (region 2 in FIG. 1a) with $\approx 1\,\text{m}$ length. A second Einzel lens (1 mm electrode separation, each with cylindrical geometry and 17 mm internal diameter) and set of deflectors (each forms a quarter of a cylinder), are situated at the end of flight region, serving to focus and steer the ions into the centre of the VMI assembly. A Photonis BiPolar ToF detector is currently positioned after the VMI assembly, although we are developing a reflectron assembly (shown in FIG. S1) to improve mass resolution and allow monitoring of photodissociation processes occurring in the VMI region.

C. Velocity-map imaging

The VMI assembly is based on a three-electrode design with low-magnetic stainless steel repeller, extractor, and ground electrodes of 120 mm diameter, 1 mm thickness, and 24 mm apertures on the extractor and ground electrodes. In a measurement, the repeller and extractor electrodes are initially grounded and are pulsed on using a second pair of Behlke switches. Laser light is timed to interact with the selected anions some nanoseconds later. Typical operating voltages are -200 to $-500\,\text{V}$ on the repeller (V_{rep}) and $\approx 0.73 V_{\text{rep}}$ on the extractor. The VMI assembly is surrounded by a cylindrical mu-metal shield (2 mm thickness, Magnetic Shields Ltd.) in order to minimize photoelectron trajectory disturbance from extraneous electric and magnetic fields. The laser light and ion packets enter the VMI region through 15 mm holes in the mu-metal shield. The ejected photoelectrons are extracted upwards and are velocity mapped onto the first of a pair of 40 mm diameter microchannel plates (MCPs) as part of a Photek VID240 detector. The second MCP is connected to a gating unit providing $+500\,\text{V}$ pulses (10 ns to $100\,\mu\text{s}$ duration), which serves to remove ion background and enables prompt vs delayed ejection processes to be quantified (FIG. 2b).[27,28] For example, if the second MCP baseline voltage is $+1000\,\text{V}$ (which provides insufficient gain to observe photoelectrons), the gating unit raises the voltage to $+1500\,\text{V}$ for duration $\mathbf{G}$ (FIG. 2a). We chose a P43 phosphor screen and glass vacuum interface as part of the VID240 detector to maximize phosphorescence signal because P43 has a high quantum yield for emission in the green, which is the spectral region where the detection efficiency of the camera sensor is maximized. The phosphor screen is monitored using a triggered Blackfly S (monochrome, Sony IMX252 CMOS) camera with a 6 mm focal length lens. The camera is held in place and isolated from room light using a 3D-printed enclosure. Photoelectron detection efficiency of the MCP is $\approx 75\%$ (limited by the open area ratio of the MCP surface), while the detection efficiency of the CMOS sensor for green light (550 nm) from the P43 phosphor is $\approx 80\%$.

The lasers available in our laboratory include a Nd:YAG pumped 20 Hz EKSPLA NT342B optical parametric oscillator (OPO) offering a wavelength range of 210–2600 nm and 4–7 ns pulse duration, a 10 Hz Quantel Nd:YAG with harmonic crystals, and a Spectra Physics Ti:Sapphire oscillator with Light Conversion optical parametric oscillators and suitable crystals offering $\approx 100\,\text{fs}$ duration femtosecond pulses. The data presented in this work was obtained using the EKSPLA NT342B laser operating at 20 Hz, with the wavelength calibrated using a Coherent WaveMaster wavemeter. The laser windows on the VMI chamber are easily changeable, with MgF_2 extended range windows mounted on $2^{3}/4$" ConFlat flanges used in this work. Pump-probe experiments with the nanosecond lasers (e.g. $1+1'$ resonance enhanced two-photon detachment) are controlled using the Quantum Composers pulse generator, while femtosecond experiments would use the Ti:Sapphire oscillator as the master clock.

D. Resolution and calibration

An example ToF spectrum averaged over 128 acquisition cycles from a hard plasma (source 1) of $<1\%$ toluene (Alfa Aesar, 99.8%) in Ar is shown in FIG. 4a. Traces of $^{79}\text{Br}^-$, $^{81}\text{Br}^-$, and $^{127}\text{I}^-$ contaminants, that were used for ToF and VMI calibration purposes, are present in the spectrum. With a total flight path of $\approx 1.3\,\text{m}$, the resolving power, $R = t/\Delta t$, where t is the flight time of the ion, and Δt is the FWHM of the signal peak, is 500–600. Calibration of the ToF spectrum was achieved using halogen anions (F^-, Cl^-, Br^-, I^-) and complexes (I_2^-, I_3^-, etc). While this resolving power is suitable for our target small molecular anions (e.g. up to 60 atoms), we will incorporate a reflectron assembly for future use, which should increase m/z resolution by approximately an order of magnitude (i.e. to ≈ 5000–6000).

An example velocity-map image, accumulated for $\approx 10\,\text{s}$, for photoelectrons ejected from I^- irradiated at 300 nm is shown in FIG. 4b, while the central slice for the symmetrized quadrant is shown in FIG. 4c. The electron kinetic energy spectrum is given in FIG. 4d, with a resolution (conventionally stated as $\Delta E/E$) of $\approx 4\%$, which is consistent with the expected performance for a three-electrode VMI assembly.[22] The resolution may be further increased with the installation of additional electrodes,[40–42] or by fabrication of a shaped repeller to flatten the imaging plane. Photoelectron images for Cl^-, Br^-, I^-, and I_2^- used to calibrate the V_{ext}:V_{rep} ratio show the optimum resolution is achieved at ratios of 0.73 or 0.74 (FIG. S2), with smaller or larger ratios exhibiting significantly reduced resolution indicated by blurring of the image rings (see FIG. S3). In addition to resolution dependence on the V_{ext}:V_{rep} ratio, the high velocity trajectories (high eKE) become unfocussed because of slight curvature of the imaging plane.
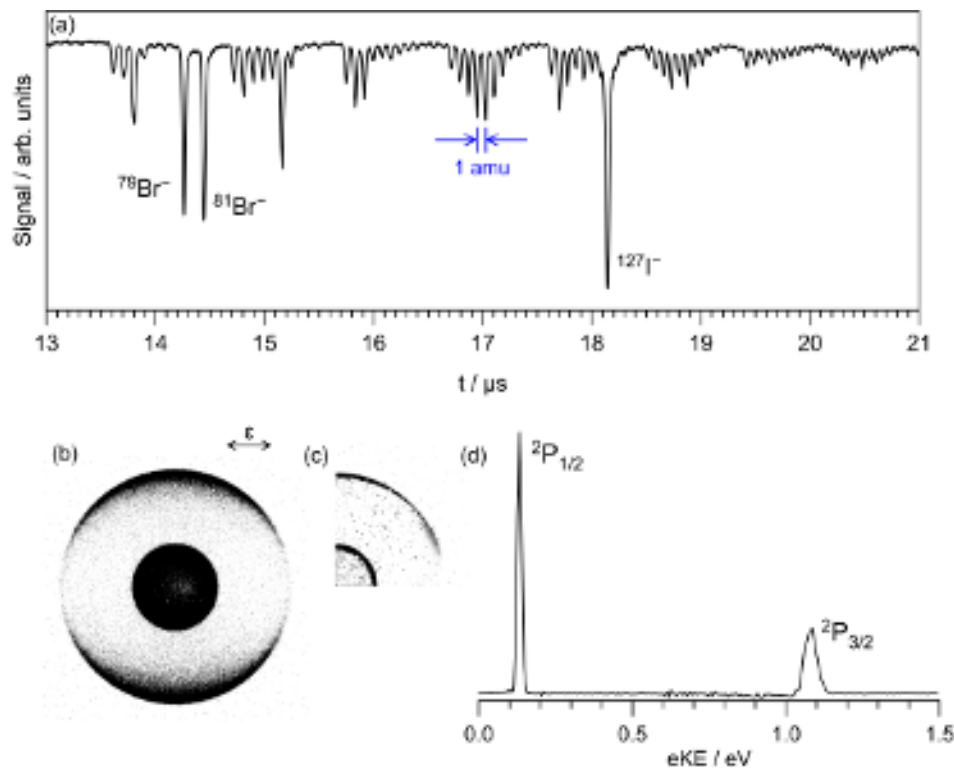
FIG. 4. ToF and VMI resolution characterization: (a) Example ToF spectrum of products formed from the plasma of <1% toluene in Ar (with traces of iodine and bromine precursors used for photoelectron spectroscopy calibration). One mass unit (1 amu) resolution is easily achieved over this mass range, with progressions of $C_nH_m^-$ species observed. The laser systems and VMI assembly can be tuned to probe to $\approx$0.1 amu precision over this mass range using typical ToF voltages. The velocity-map images were recorded under operating conditions of $V_{MCP} = +1200$ V (with +500 V gate) and $V_{phos} = +4$ kV. A mass spectrum extending out to $m/z \approx 600$ is shown in the Supplementary Material (FIG. S4). (b) Crushed velocity-map image for photoelectrons emitted from I^- irradiated at 300 nm. ε indicates the laser polarization axis. (c) Central slice for the symmetrized image quadrant as part of the VMI reconstruction procedure using polar onion peeling.[37] (d) Extracted photoelectron spectrum with electron kinetic energy (eKE); resolution $\frac{\Delta E}{E} \approx 4\%$. Energy is calibrated by converting pixels to electron kinetic energy, taking into account the photon energy and energy levels from the NIST database for the $^2P_{1/2}$ and $^2P_{3/2}$ terms.

E. CH_2CN^-

Operation of the instrument is demonstrated through simultaneous acquisition of photodetachment and photoelectron data for jet-cooled CH_2CN^- produced, using a mixture of $\approx$0.5% CH_3CN (Fisher Scientific, >99%) in air, with plasma source 2; this source produced near-exclusively CN^- and CH_2CN^-. These acquisitions involved an estimated 10^6 anions per ToF cycle (20 Hz) crossed with the EKSPLA laser focussed to $\approx$1.5 mm diameter with 2–3 mJ pulse^{-1}. The anion beam was focussed using the Einzel lenses to have a similar radial extent to the laser (as checked by vertically moving the laser beam over the ion packet). Resolution of the photodetachment spectra is limited by the laser bandwidth.

CH_2CN^- is an appealing target for demonstration because it supports a dipole-bound state (DBS) with rovibrational structure, and has several low-energy temporary anion resonances situated in the detachment continuum. Briefly, the DBS is a non-valence state of an anion,[7] in which an electron is bound beyond a molecule's valence shell by the electric field associated with the dipole moment, μ, of the neutral core, provided $\mu > 1.625$ D.[43] Despite a typical DBS being bound by only 10–100 meV, they can play a critical role in excited-state dynamics following internal conversion from valence-localized states,[18,44,45] and in processes ranging from interstellar anion formation to radiation-induced DNA damage.[46,47] Temporary anions or resonances are quasi-bound states situated in the detachment continuum, but are temporarily bound (valence-localized) through some combination of polarization, exchange, and centrifugal forces.[1,7,48] In essence, these states correspond to 'conventional' excited states of the anion.

The complete photodetachment spectrum recorded for CH_2CN^- is shown in FIG. 5a (11904–24390 cm^{-1}), with panels (b)–(d) expanding regions of interest. In brief, a series of sharp rovibronic peaks (K-bands) associated with the DBS are observed just below and above the detachment threshold (12300–12600 cm^{-1} and 12850–13100 cm^{-1}, respectively), while broad vibrational structure is observed over the 19000–24390 cm^{-1} range (asso-
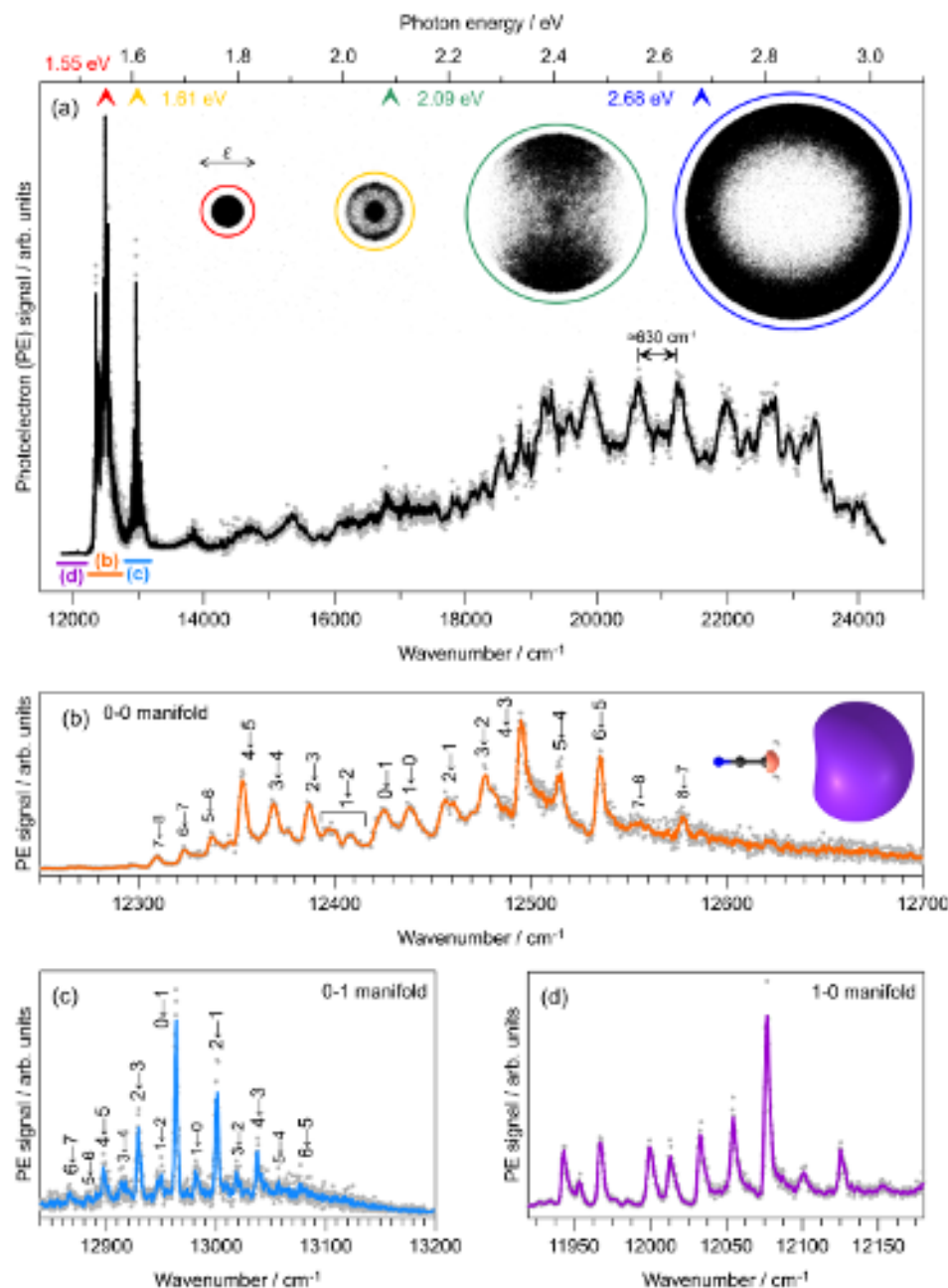
FIG. 5. Photodetachment spectra and selected photoelectron velocity-map images of CH_2CN^-: (a) Full spectrum with selected photoelectron velocity-map images to show changes in anisotropy over the 19000–24000 cm^{-1} region. ε indicates the polarization axis of the laser with respect to the images. The full photodetachment spectrum, including over 5000 velocity-map images (photoelectron spectra), were recorded over the period of one week. The grey dots are the raw data, and the solid line is five-point running average. The regions of the panels (b)-(d) are shown in panel (a). (b) Expansion of the dipole-bound state and 0-0 vibrational manifold showing rotational K-bands, with assignments following Refs 38,39. (c) Expansion of the 12300–13200 cm^{-1} region (0-1 vibrational manifold) with assigned rotational K-bands. (d) Weak hot band signal (1-0 vibrational manifold). Spectral assignments are tabulated in the Supplementary Material. The calculated dipole-bound state (DBS) orbital (EA-EOM-CCSD/aug-cc-pVDZ+8spd level of theory, 0.0035 a.u. isosurface) is shown inset in (b). The computed DBS binding energy is 90 cm^{-1} (valance anion equilibrium geometry) and 78 cm^{-1} (neutral equilibrium geometry) – see Supplementary Material for further details. The laser bandwidth was $\approx$4 cm^{-1}.

ciated with valence-localized resonances). The 12600–12280 cm^{-1} region, shown in FIG. 5b, is assigned to groups of transitions from the lowest vibrational level of the anion to the lowest vibrational level of the DBS that may detach *via* rotational-electronic coupling.[38,39] The spectrum resembles earlier published results,[38,39,49] although the anions in our measurements have substantially lower temperature due to jet-cooling on supersonic expansion. A complete assignment of the rovibronic bands is given in the Supplementary Material. The following discussion provides a brief interpretation of the spectrum since it represents the clearest photodetachment spectrum for CH_2CN^- to date and spans over 12,000 cm^{-1} in a single acquisition.

Transitions associated with the 0-1 manifold (i.e. to the first vibrational excited state of the DBS) are shown expanded in FIG. 5c. As discussed in Ref. 39, the manifold shows a difference in K-band intensities compared with the 0-0 manifold in FIG. 5b because all DBS levels for the 0-1 manifold are above the detachment threshold and may promptly autodetach. The difference in K-band intensities is more evident in our work compared with earlier works[39,49] due to the lower anion temperatures here. The intensity pattern reflects the expected nuclear spin statistics, where transitions from an odd K level of the ground state anion are three times more intense than those from an even K ground state.[50] In essence, for the 0-1 manifold, the substantial change in geometry between anion and neutral provides a vibrationally-mediated electron ejection where the umbrella motion (protons wagging above and below the plane) modulates the DBS orbital.[51] We determine the umbrella mode frequency to be 430 ± 10 cm^{-1}, which is in good agreement with an anharmonic frequency calculation value of 433 cm^{-1} (ωB97X-D/aug-cc-pVTZ).

Although our anions are jet-cooled in a supersonic expansion, trace hot band signal (1-0 manifold) from a vibrationally excited state of the anion to the lowest vibrational state of the DBS was observed (FIG. 5d). We have not attempted K-band assignment for this region. While this signal is low, from our experimental point of view, it is easy to increase the gain of the MCP detector in order to measure reliable photodetachment spectra for extremely weak signals.

The photodetachment spectrum between 13,500–18,000 cm^{-1} shows a series of weak, broad features attributed to direct photodetachment to the ground electronic state of the neutral. The velocity-map images in this region are highly anisotropic ($\beta_2 \approx +2$), consistent with s or d-wave detachment from a p-like orbital, and show a series of rings linked with vibrational states of the neutral (assigned below). Between 18,000–24,000 cm^{-1}, the photodetachment spectrum shows a series of peaks with ≈630 cm^{-1} spacing and ≈300 cm^{-1} width (corresponding to ≈10 fs lifetime). Velocity-map images corresponding to excitation resonant with the peak features reveal near isotropic rings ($\beta_2 \approx +0.1$ to $+0.2$) with a much narrower velocity distribution

than images non-resonant with the peak features where $\beta_2 \approx +2$ (photoelectron spectra are given in the next section), and thus show distinct electron detachment dynamics. CAP-EOM-CCSD/aug-cc-pVTZ vertical excited state calculations for the anion determine a temporary anion resonance, $S_1(A')$ with shape resonance character (HOMO[p]$\rightarrow$LUMO[π^*]), situated at 2.52 eV (oscillator strength, $f = 0.034$), while IP-EOM-CCSD/aug-cc-pVTZ calculations of ionized (neutral) states show that they all lie well beyond the spectral range considered in this work. We thus assign the vibrational structure over the 18,000–24,000 cm^{-1} range to prompt autodetachment from the temporary anion S_1 electronic state. An EOM-CCSD/aug-cc-pVTZ geometry optimization of the S_1 state reveals essentially planar C_s symmetry, and harmonic frequency analysis determined the umbrella mode at 611 cm^{-1}, which is consistent with the experimental vibrational spacing (≈630 cm^{-1}). To our knowledge, this is the first characterization of the S_1 state for CH_2CN^-. It is worth noting that photoexcitation cross-sections to resonances typically have higher cross-sections than direct photodetachment; therefore, the former processes dominate photodetachment spectra.

F. 2D photodetachment-photoelectron spectroscopy

A major advantage of our instrument is that velocity-map images, providing photoelectron spectra and angular distributions, and the photodetachment spectrum are acquired simultaneously. In practice, we first perform a survey photodetachment scan over the desired spectral range to gauge total signal levels. This also guides subdivision of the higher-resolution acquisitions into suitable blocks, allowing maximization of signal level while avoiding saturation and multiphoton processes (resonant two-photon detachment or sequential absorptions).

A 2D photodetachment-photoelectron map over the $h\nu$=1.908–3.024 eV (15386–24392 cm^{-1}) photon energy range is shown in FIG. 6a with the photodetachment spectrum in FIG. 6b, to allow correlation of 2D map features with spectral features. The 2D plot is usually presented in terms of photon energy (eV) rather than wavenumber so as to be consistent with the eKE dimension given in units of eV. In quantitative terms, the 2D map in FIG. 6a was constructed from 2401 individual photoelectron spectra, with each individual spectrum averaged over three or four acquisitions (of 2 s or 40 laser shots each). Thus, each summed velocity-map image and photoelectron spectrum corresponds to 6–8 s of acquisition or 120–160 image frames. This number of frames is roughly the 'minimum' required for a reasonable signal-to-noise velocity-map image after reconstruction. In terms of acquisition throughput, our photoelectron spectra at a given photon energy, which were recorded in less than 10 s each, are of similar quality to a study that reported only a single photoelectron spectrum for CH_2CN^-.[52] The 2D map presented in FIG. 6a excludes
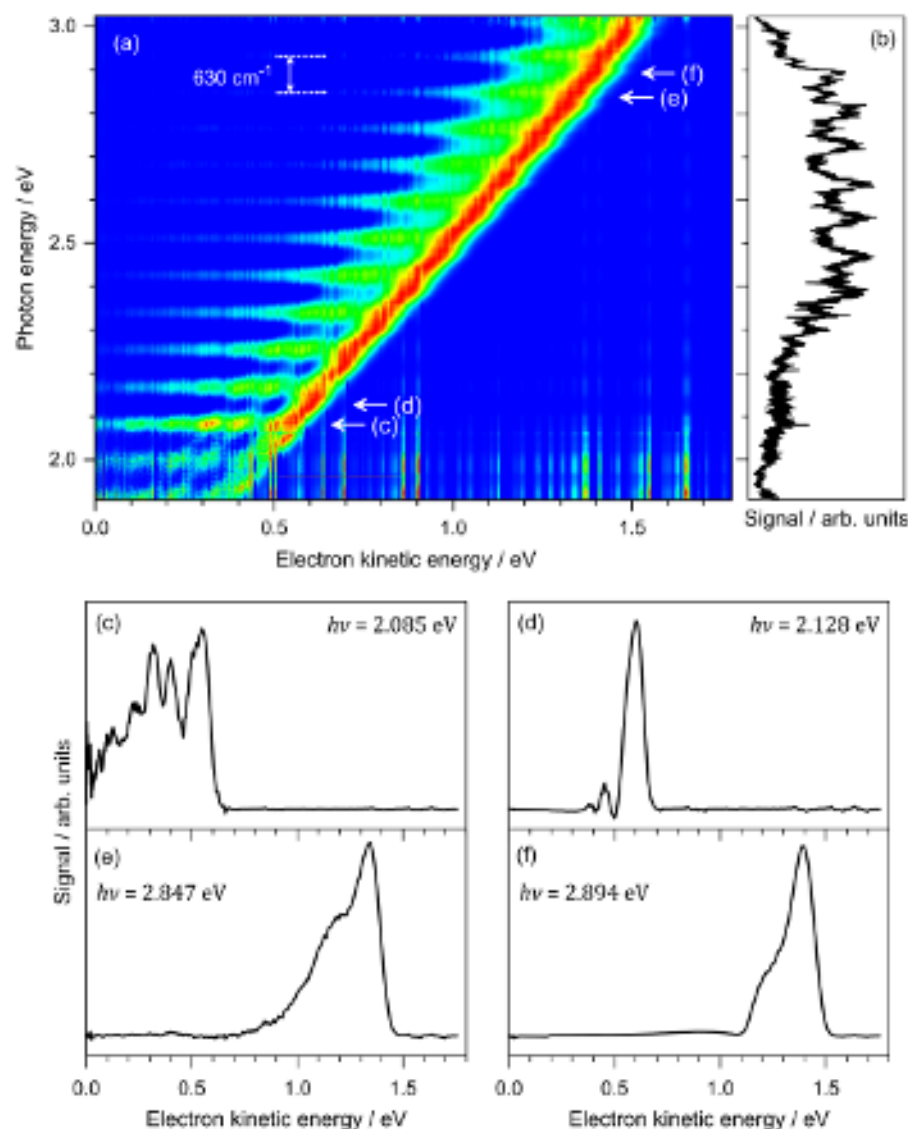
FIG. 6. 2D photodetachment-photoelectron spectroscopy of CH_2CN^-: (a) 2D map over the $h\nu$=1.908–3.024 eV (15386–24392 cm^{-1}) photon energy range. The 2D map was constructed from 2401 individual spectra, with each photoelectron spectrum normalized to have unit maximum signal intensity in order to accentuate spectral features. For photon energies over the $h\nu$=1.9–2.1 eV range, the photodetachment cross section is low and signal-to-noise in the photoelectron spectra is poorer (the vertical lines at photon energies below $\approx$2.2 eV are because of low signal-to-noise). (b) Photodetachment spectrum over the same range from FIG. 5a (five-point moving average). (c)–(f) Selected photoelectron spectra at given photon energies. $h\nu$=2.085 and 2.847 eV ($\beta_2 \approx$+2) are dominated by direct photodetachment, while $h\nu$=2.128 and 2.894 eV ($\beta_2 \approx$+0.1 to +0.2) are dominated by prompt autodetachment from the S_1 electronic state of the anion. Each photoelectron spectrum was extracted from a velocity-map image recorded in less than 10 s. The optimization of signal is important for high-throughput photoelectron spectroscopy.

data recorded over the DBS rovibrational features, which would expand the 2D map to include >5000 individual spectra.

The 2D map shows a clear, systematic oscillation in high-eKE and lower-eKE photoelectron features with increasing photon energy, consistent with the $\approx$630 cm^{-1} peak spacing observed in the photodetachment spectrum. The vibrational progression associated with the autodetaching $S_1 \leftarrow S_0$ transition is extended because of the

substantial differences in geometry between the bent and planar geometries. Selected photoelectron spectra are shown in FIG. 6c–f. These spectra show that photon energies not resonant with $S_1 \leftarrow S_0$ vibronic transitions (FIG. 6a and c) have a more extended eKE distribution with the photoelectron spectra showing a series of vibrational states, similar to the spectra reported and assigned in Ref. 53. On the other hand, the photoelectron spectra resonant with $S_1 \leftarrow S_0$ vibrations (FIG. 6d and f) are

dominated by a single lifetime-broadened autodetaching vibration, reflecting the coupling between the umbrella mode vibrations in the S_1 state and the detached D_0 state.

While the presented 2D map highlights the difference between direct photodetachment and prompt autodetachment processes, similar experiments on larger molecular anions, such as biochromophores, show increased complexity due to further competing pathways and multiple (potentially overlapping) excited states.[1,6,54] Trends in these 2D maps over vibrational progressions provide detailed insights into the excited-state dynamics. The 2D photodetachment-photoelectron spectroscopy strategy applied to CH_2CN^- is applicable to any molecular anion that can be generated in our instrument.

III. CONCLUSION AND FUTURE DIRECTIONS

We have successfully deployed an instrument to perform photodetachment and photoelectron spectroscopy of gas-phase anions generated in pulsed plasma sources. The construction of the experiment, using standard 6" and $2^3/4$" ConFlat flanges and the use of 3D printable mounts and holders allows the instrument to be adapted easily to incorporate a variety of ion sources or additional sectors as applications demand. The application of high-throughput 2D photodetachment-photoelectron spectroscopy of jet-cooled molecular anions, as demonstrated here for CH_2CN^-, is suitable for a wide range of systems, including anions important in the interstellar medium, and anions (and hydrated clusters) relevant in various regions of the atmosphere. We are studying such systems presently.

There are two directions for future development. First, a femtosecond laser available in our laboratory will be integrated with the instrument to allow for pump-probe time-resolved spectroscopy.[1,11] Second, we are deploying another section of the instrument, which includes electrospray ionization, tandem ion mobility spectrometry, and ion trapping using a 3D Paul trap. While both sections could be operated independently, the merging of the two instrument sections will enable larger, more fragile, biomolecules to be mass- and shape-selected and, subsequently, probed *via* photoelectron, photodetachment, and photodissociation action spectroscopy. This second section will also enable photoisomerization action spectroscopy, which is a novel strategy for directly monitoring isomerization in the gas-phase.[55] Additionally, we will be able to photo- or collisionally generate and isolate transient species, such as unstable *Z*-isomers or tautomers that are otherwise not possible to study unequivocally.[56,57]

SUPPLEMENTARY MATERIAL

The Supplementary Material contains details on: Further CAD illustrations of the instrument, Illustration of the gas-inlet manifold, Behlke switch pulsing circuits, ToF spectrum showing m/z up to 750, Further velocity-map images, Illustration of future developments including tandem ion mobility and ion trapping, Computational chemistry methods, Assignment of rovobronic structure of the DBS and wavenumbers for the rovibronic transitions.

DATA AVAILABILITY

The data that support the findings of this study are available from the corresponding author upon reasonable request.

ACKNOWLEDGMENTS

CONFLICTS OF INTEREST

The authors have no conflicts to disclose.

REFERENCES

[1] C. S. Anstöter, J. N. Bull, and J. R. R. Verlet, Int. Rev. Phys. Chem. **35**, 509 (2016).

[2] A. Henley and H. H. Fielding, Int. Rev. Phys. Chem. **38**, 1 (2019).

[3] L.-S. Wang, J. Chem. Phys. **143**, 040901 (2015).

[4] J. Simons, J. Phys. Chem. A **127**, 3940 (2023).

[5] C. J. Clarke and J. R. R. Verlet, Ann. Rev. Phys. Chem. **75**, 89 (2024).

[6] J. N. Bull, C. W. West, and J. R. R. Verlet, Chem. Sci. **6**, 1578 (2015).

[7] J. Simons, J. Phys. Chem. A **112**, 6401 (2008).

[8] D. H. Parker and A. T. J. B. Eppink, Velocity map imaging: applications in molecular dynamics and experimental aspects, in *Imaging in Molecular Dynamics* (Cambridge University Press, 2003) pp. 20–64.

[9] X.-B. Wang and L.-S. Wang, Rev. Sci. Instrum. **79**, 073108 (2008).

[10] A. B. Wolk, C. M. Leavitt, E. Garand, and M. A. Johnson, Acc. Chem. Res. **47**, 202 (2013).

[11] A. Kunin and D. M. Neumark, Femtosecond time-resolved photoelectron spectroscopy of molecular anions, in *Physical Chemistry of Cold Gas-Phase Functional Molecules and Clusters* (Springer Singapore, 2019) pp. 307–335.

[12] X.-B. Wang and L.-S. Wang, Ann. Rev. Phys. Chem. **60**, 105 (2009).

[13] O. T. Ehrler and D. M. Neumark, Acc. Chem. Res. **42**, 769 (2009).

[14] X.-B. Wang, J. Phys. Chem. A **121**, 1389 (2017).

[15] A. Svendsen, H. V. Kiefer, H. B. Pedersen, A. V. Bochenkova, and L. H. Andersen, J. Am. Chem. Soc. **139**, 8766 (2017).

[16] R. E. Continetti and H. Guo, Chem. Soc. Rev. **46**, 7650 (2017).

[17] M. S. Schuurman and V. Blanchet, Phys. Chem. Chem. Phys. **24**, 20012 (2022).

[18] J. N. Bull, C. S. Anstöter, M. H. Stockett, C. J. Clarke, J. A. Gibbard, E. J. Bieske, and J. R. R. Verlet, J. Phys. Chem. Lett. **12**, 11811 (2021).

[19] D. H. Kang, J. Kim, H. J. Eun, and S. K. Kim, Acc. Chem. Res. **55**, 3032 (2022).

[20] G.-Z. Zhu and L.-S. Wang, Chem. Sci. **10**, 9409 (2019).

[21] A. Sanov, Annu. Rev. Phys. Chem. **65**, 341 (2014).

[22] A. T. J. B. Eppink and D. H. Parker, Rev. Sci. Instrum. **68**, 3477 (1997).

[23] V. D. Belov and M. I. Yavor, Nucl. Instrum. Methods Phys. Res. A **470**, 105 (2001).

[24] H. U. Poll, C. Winkler, D. Margreiter, V. Grill, and T. D. Märk, Int. J. Mass Spectrom. Ion Processes **112**, 1 (1992).

[25] M. Yavor, in *Advances in Imaging and Electron Physics* (Elsevier, 2009) pp. 213–258.

[26] D. M. Neumark, J. Phys. Chem. A **112**, 13287 (2008).

[27] B. Concina and C. Bordas, J. Phys. Chem. A **126**, 7442 (2022).

[28] J. N. Bull, C. W. West, and J. R. R. Verlet, Phys. Chem. Chem. Phys. **17**, 32464 (2015).

[29] F. W. McLafferty, ed., *Mass spectrometry of organic ions* (Academic Press, New York, 1963).

[30] C. Jouvet, C. Lardeux-Dedonder, and D. Solgadi, Chem. Phys. Lett. **156**, 569 (1989).

[31] K. N. Rosser, Q.-Y. Wang, and C. M. Western, J. Chem. Soc., Faraday Trans. **89**, 391 (1993).

[32] D. L. Osborn, D. J. Leahy, D. R. Cyr, and D. M. Neumark, J. Chem. Phys. **104**, 5026 (1996).

[33] I. Alata, R. Omidyan, C. Dedonder-Lardeux, M. Broquier, and C. Jouvet, Phys. Chem. Chem. Phys. **11**, 11479 (2009).

[34] I. Alata, R. Omidyan, M. Broquier, C. Dedonder, and C. Jouvet, Chem. Phys. **399**, 224 (2012).

[35] J. C. Loison, C. Dedonder-Lardeux, C. Jouvet, and D. Solgadi, Faraday Discuss. **97**, 379 (1994).

[36] W. C. Wiley and I. H. McLaren, Rev. Sci. Instrum. **26**, 1150 (1955).

[37] G. M. Roberts, J. L. Nixon, J. Lecointre, E. Wrede, and J. R. R. Verlet, Rev. Sci. Instrum. **80**, 053104 (2009).

[38] K. R. Lykke, D. M. Neumark, T. Andersen, V. J. Trapa, and W. C. Lineberger, J. Chem. Phys. **87**, 6842 (1987).

[39] D. M. Wetzel and J. I. Brauman, J. Chem. Phys. **90**, 68 (1989).

[40] I. León, Z. Yang, H.-T. Liu, and L.-S. Wang, Rev. Sci. Instrum. **85**, 083106 (2014).

[41] S. J. Kregel, G. K. Thurston, J. Zhou, and E. Garand, J. Chem. Phys. **147**, 094201 (2017).

[42] E. Sakkoula, B. G. M. van Oorschot, and D. H. Parker, Mol. Phys. **120**, e1910357 (2021).

[43] E. Fermi and E. Teller, Phys. Rev. **72**, 399 (1947).

[44] J. N. Bull, C. W. West, and J. R. R. Verlet, Chem. Sci. **7**, 5352 (2016).

[45] J. N. Bull, C. S. Anstöter, and J. R. R. Verlet, Nat. Comm. **10**, 5820 (2019).

[46] T. J. Millar, C. Walsh, and T. A. Field, Chem. Rev. **117**, 1765 (2017).

[47] L. Sanche, Eur. Phys. J. D **35**, 367 (2005).

[48] K. D. Jordan and P. D. Burrow, Chem. Rev. **87**, 557 (1987).

[49] J. Marks, D. M. Wetzel, P. B. Comita, and J. I. Brauman, J. Chem. Phys. **84**, 5284 (1986).

[50] H. W. Kroto, *Molecular rotation spectra* (Dover Publications, 2003) p. 311.

[51] J. Simons, J. Am. Chem. Soc. **103**, 3971 (1981).

[52] D. J. Goebbert, L. Velarde, D. Khuseynov, and A. Sanov, J. Phys. Chem. Lett. **1**, 792 (2010).

[53] S. Moran, H. B. Ellis Jr., D. J. DeFrees, A. D. McLean, and G. B. Ellison, J. Am. Chem. Soc. **109**, 5996 (1987).

[54] C. W. West, J. N. Bull, A. S. Hudson, S. L. Cobb, and J. R. R. Verlet, J. Phys. Chem. B **119**, 3982 (2015).

[55] B. D. Adamson, N. J. A. Coughlan, P. B. Markworth, R. E. Continetti, and E. J. Bieske, Rev. Sci. Instrum. **85**, 123109 (2014).

[56] J. N. Bull, M. S. Scholz, E. Carrascosa, G. da Silva, and E. J. Bieske, Phys. Rev. Lett. **120**, 223002 (2018).

[57] J. N. Bull, E. Carrascosa, N. Mallo, M. S. Scholz, G. da Silva, J. E. Beves, and E. J. Bieske, J. Phys. Chem. Lett. **9**, 665 (2018).